

1 **Segmentation of Storm Enhanced Density (SED) by**
2 **Boundary Flows Associated with Westward Drifting**
3 **Partial Ring current**

4 **Zihan Wang¹, Shasha Zou¹, Thomas Coppeans¹, Jiaen Ren¹, Aaron Ridley¹,**
5 **Tamas Gombosi¹**

6 ¹Department of Climate and Space Sciences and Engineering, University of Michigan, Ann Arbor, MI,
7 United States

8 **Key Points:**

- 9 • Boundary flows between Region-1 and Region-2 FACs segment SED plume into
10 a patch.
11 • Localized plasma loss due to enhanced frictional heating within boundary flows.
12 • No external IMF direction change needed in this segmentation scenario.

This is the author manuscript accepted for publication and has undergone full peer review but has not been through the copyediting, typesetting, pagination and proofreading process, which may lead to differences between this version and the [Version of Record](#). Please cite this article as doi: [10.1029/2019GL084041](https://doi.org/10.1029/2019GL084041)

Corresponding author: Zihan Wang, wzihan@umich.edu

Abstract

The segmentation mechanism of polar cap patches is agreed to be related to temporal changes of IMF or transient reconnection. In this letter, using GITM driven by two-way coupled Block-Adaptive-Tree-Solarwind-Roe-Upwind-Scheme (BATSRUS) and Rice Convection Model (RCM), a new segmentation mechanism is proposed. This mechanism works as follows: a strong boundary flow between the Region 1 and Region 2 Field-Aligned Currents (FACs) develops while a shielding process develops in the inner magnetosphere. As the partial ring current drifts westward, the peak of the boundary flow also moves westward. This strong boundary flow raises the ion temperature through enhanced frictional heating, enhances the chemical recombination reaction rate and reduces the electron density. When this boundary flow crosses the Storm-Enhanced Density (SED) plume, the plume will be segmented into patches. No external IMF variations or transient reconnections are required in this mechanism.

1 Introduction

Polar cap patches are high F-region plasma density structures in the polar cap where the density is much higher than the background level. Both Storm Enhanced Density (SED) and patches have drawn much attention since their discoveries, because the large density gradient at their edges is favorable for ionospheric irregularities to develop. Thus they are the major space weather concern in the polar cap that can disrupt navigation and communication signals during times of geomagnetic disturbance.

Various formation mechanisms of patch segmentation have been proposed and it is still controversial which mechanism is the dominant one. However, it is typically believed that the formation of patch needs a reservoir of high-density plasma and a segmentation mechanism. There are two sources of high-density plasma: The first source is the plasma density increase in the cusp due to soft precipitation in the F region (Goodwin et al., 2015; Rodger, Pinnock, Dudeney, Baker, & Greenwald, 1994; Walker, Moen, Kersley, & Lorentzen, 1999). The second source is the dense thermal plasma from the sunlit region (Anderson, Buchau, & Heelis, 1988). SED is a ridge of enhanced electron density in the mid-latitude region that forms during storm time (Foster, 1993), and is considered to be an important plasma source for patches. Ren, Zou, Gillies, Donovan, and Varney (2018) show that the altitude profiles of patch density and temperature resemble those of SED. That is, the patch density is usually higher than the sector median above 200 km and lower than that below 200 km, and the patch electron temperature is lower than the surrounding region. This is strong evidence that patches originate from SED.

The dense plasma of SED can be transported into the high-latitude region to form SED plume or Tongue of Ionization (TOI) (Foster, 1984). To isolate the plume into patches, a segmentation mechanism is needed. It is generally believed that the segmentation is closely related with IMF variations. Patches can be segmented due to the temporal changes in both IMF Bz (Anderson et al., 1988) and By (Milan, Lester, & Yeoman, 2002; Sojka et al., 1993). Patches can also be generated by Flux Transfer Events (FTE) near the cusp region (Carlson et al., 2006; Carlson, Oksavik, Moen, & Pedersen, 2004; Lockwood & Carlson, 1992). FTE can lead to meso-scale (about 100 km) fast flow channels near the cusp (Oksavik et al., 2006; Pinnock et al., 1993) and then bring dense plasma into the polar cap region (Lockwood & Carlson, 1992; Rodger et al., 1994; Zhang et al., 2011). Moen et al. (2006) further show that pulsed return flow due to transient reconnection can chop the plume into patches in the subauroral region. Another possibility is that fast flow jets due to transient reconnection produce high-temperature and low-density plasma through frictional heating and erode the pre-existing plume into patches (Ogawa, Buchert, Nishitani, Sato, & Lester, 2001; Valladares, Basu, Buchau, & Friis-Christensen, 1994; Valladares, Decker, Sheehan, & Anderson, 1996). Zhang et al. (2013) further show that

64 the low-density plasma due to precipitation can segment the TOI into patches during
65 transient reconnection. Zhang et al. (2016) show that Subauroral Polarization Streams
66 (SAPS) can transport low-density plasma from the night side to cut the SED during a
67 substorm.

68 In this letter, Global Ionosphere Thermosphere Model (GITM) was used to sim-
69 ulate the geomagnetic storm on Sep 7, 2017 and study the segmentation of SED plume
70 into a polar cap patch. GITM is driven by high-resolution coupled Block-Adaptive-Tree-
71 Solar Wind-Roe-Upwind-Scheme (BATSRUS) and Rice Convection model (RCM) within
72 the Space Weather Modeling Framework (SWMF) (Tóth et al., 2005; Tóth et al., 2012).
73 Our results are not only consistent with observations, but also for the first time show
74 that a strong boundary flow can form between the Region 1 and Region 2 FACs during
75 the shielding development and westward drift of partial ring current in the inner mag-
76 netosphere, and this flow can reduce the electron density and segment SED plume into
77 a patch.

78 2 Observations and Modeling

79 2.1 Model Description

80 GITM is a three-dimensional spherical grid that models the Earth's global iono-
81 sphere and thermosphere system self-consistently (Ridley, Deng, & Tóth, 2006). In this
82 study, the spatial resolution of GITM is set to 1 degree in latitude and 2 degree in lon-
83 gitude with 50 vertical levels (from ~ 100 to ~ 700 km). GITM allows different mod-
84 els of high-latitude electric fields, auroral particle precipitation, and solar radiation as
85 inputs. In this study, the Flare Irradiance Spectral Model (FISM) (Chamberlin, Woods,
86 & Eparvier, 2007, 2008) is used to provide solar irradiance input for the whole simula-
87 tion. FISM is an empirical model of the solar irradiance spectrum covering from 0.1 to
88 190 nm with 1 nm resolution and 1-minute temporal resolution. Using the high-resolution
89 FISM model, the solar flare impact on the ionosphere and thermosphere can be captured.

90 Various models of high-latitude electric fields and auroral particle precipitation can
91 be used in GITM. At first, GITM was run for two quiet days (Sep 4-5) to achieve steady
92 state. During this stage, the Fuller-Rowell and Evans empirical model (Fuller-Rowell &
93 Evans, 1987) and Weimer empirical electric field model (Weimer, 2005) are used as the
94 precipitation and electric field input, respectively. The Fuller-Rowell and Evans model
95 is driven by Hemispheric Power (HP), which is found to be linearly related with $AL^{\frac{1}{2}}$
96 in Østgaard, Vondrak, Gjerloev, and Germany (2002) empirical model. We use the ob-
97 served AL index from the Kyoto WDC to calculate the hemispheric power. The Weimer
98 model is driven by the observed solar wind data from OMNIWeb. Starting from Sep 6
99 00 UT, the high-latitude driver is switched to the electric field and precipitation from
100 the 2-way coupled BATSRUS and RCM models, as part of the University of Michigan
101 Space Weather Modeling Framework (SWMF) (De Zeeuw et al., 2004; Tóth et al., 2012).
102 The coupled model is driven by the real solar wind data from OMNIWeb. High resolu-
103 tion grid ($1/8R_E$) in the inner magnetosphere, magnetopause and current sheet has been
104 implemented to better capture dynamic FACs and precipitation structures.

105 2.2 Solar Wind and IMF

106 An intense double-dip geomagnetic storm occurred at Sep 7-8, 2017 and has received
107 much attention (e.g. Aa et al., 2018; Jin et al., 2018). The SYM-H index reached -142
108 nT during the first dip and then \sim -100 nT during the second dip. The double-dip storm
109 was driven by multiple interplanetary coronal mass ejections (ICMEs) passing the Earth
110 successively (Shen, Luo, Chi, Xu, & Wang, 2018). From top to bottom, Figure 1a-1f shows
111 the Interplanetary Magnetic Field (IMF) B_y , B_z in GSM coordinates, solar wind speed,
112 proton number density, dynamic pressure and the SYM-H index during Sep 7-8, 2017.

113 The IMF Bz turned southward at ~ 2040 UT on Sep 7 due to the arrival of the first ICME,
114 leading to the initial decrease of SYM-H. At ~ 2330 UT, a shock-ICME complex struc-
115 ture arrived with the shock enhanced IMF Bz reaching ~ -30 nT. A sudden storm com-
116 mencement signaled by the sudden SYM-H increase was also initiated by this shock. Af-
117 ter that, the SYM-H continued to decrease due to the large southward IMF and reached
118 the first minimum at ~ 0100 UT. Then the storm began to recover until the arrival of
119 another ICME at ~ 1105 UT on Sep 8, which led to the second main phase. In this study,
120 we focus on the development and structuring of SED during the first main phase. In Fig-
121 ure 1f, the dashed line represents the simulated Dst index. Although there is a ~ 20 nT
122 negative bias, the temporal variation of the simulated Dst is consistent with the SYM-
123 H index.

124 2.3 Model Results

125 The SED formation and patch segmentation processes are shown in Figure 2, and
126 the color-coded vertical dashed lines in Figure 1 indicate the timing of the three snap-
127 shots (2100 UT, 2130 UT and 2300 UT). The first row shows the GPS TEC in geomag-
128 netic coordinates. It is shown that the SED and the plume began to develop after the
129 southward turning of IMF, and the segmentation of the plume occurred at 2300 UT. The
130 bottom three rows in Figure 2 show the dynamical evolution of the ionosphere and in-
131 ner magnetosphere from SWMF after the first southward turning. The second row shows
132 the GITM electron density at 349.4 km with color contours and electric equipotential
133 line contours every 10^4 V in geomagnetic coordinates centered at the Magnetic North
134 Pole. The third row shows the SWMF FACs with color contours and the same electric
135 equipotential contours every 10^4 V in geomagnetic coordinates. The green dashed line
136 represents the open-closed field line boundary (OCB). The bottom row shows the plasma
137 pressure in the XY plane at Z=0 in GSM coordinates. Movies of GPS TEC, electron den-
138 sity at 350 km, FACs and plasma thermal pressure are provided in the supporting in-
139 formation. Based on the comparison between the first and second row in Figure 2, it is
140 shown that the simulation results successfully captured the development of the SED and
141 plume after 2100 UT, and the segmentation of plume at 2300 UT.

142 As shown in Figure 1, the IMF Bz turned southward at 2040 UT on Sep 7, reach-
143 ing -10 nT at 2100 UT, and stayed steadily southward for about 2.5 hours until the shock
144 arrival at 2330 UT. Due to this southward turning, a two-cell convection pattern started
145 to form and the convection electric field penetrated to mid-latitudes. The convection also
146 tilted towards the dawn side, which is likely due to the long lasting positive IMF By (Weimer,
147 2005). In the equatorial plane of the inner magnetosphere, a weak nearly symmetric ring
148 current can be seen at 21 UT. Both the Region 1 and Region 2 FACs existed. However,
149 the Region 2 FACs were weaker than the Region 1 FACs, because of weak partial ring
150 current. The penetrated electric field was able to reach the plasma in the sunlit mid-latitude
151 region. Both the two-cell convection pattern and OCB expanded to lower latitude. More
152 plasma in the mid-latitude followed the convection to higher latitude. Because the mag-
153 netic field is not strictly vertical in subauroral and auroral region, the convection flow
154 had an upward component and transported plasma to higher altitude, where the charge
155 exchange and recombination rate is lower (Heelis, Sojka, David, & Schunk, 2009; Zou
156 et al., 2014, 2013). This lifting and horizontal advection led to the transport of increased
157 electron density.

158 At 2130 UT, more plasma was transported from the plasma sheet to the inner mag-
159 netosphere due to the steady southward IMF, and the partial ring current developed on
160 the night side. Because of the increase of the convection electric field, the plasma in the
161 dayside ring current was not in a closed drift path anymore and thus drifted sunward
162 to the magnetopause, which led to the disappearance of ring current on the day side. To-
163 gether with continued buildup of ring current on the night side, the partial ring current
164 formed with larger azimuthal pressure gradient and thus stronger Region 2 FACs accord-

165 ing to the Vasyliunas equation (Vasyliunas, 1970). This led to stronger Region 2 FACs
166 which flowed up from the dawnside ionosphere and down into the duskside. The partial
167 ring current charged up positive on the duskside and negative in the dawnside to sup-
168 port the Region 2 FAC (Wolf, Spiro, Sazykin, & Toffoletto, 2007). This charge separa-
169 tion generated a dawnward electric field, which was opposite to the convection electric
170 field. This is referred to as the shielding phenomenon. During this period, the shield-
171 ing effect began to grow. The electron density in the mid-latitude SED base region can
172 continue to grow as long as the convection electric field there is not completely shielded,
173 and a local maximum of electron density is created (see the electron density at 2130 UT
174 in Figure 2). The high-density plasma then drifted further northward and into the pol-
175 ar cap region.

176 At 2300 UT, the IMF B_z had been steadily southward for two hours. A strong partial
177 ring current built up due to the persistent and strong transport from the plasma sheet
178 to the inner magnetosphere. The peak pressure reached ~ 20 nPa and the pressure gra-
179 dient generated much stronger Region 2 FACs. Due to the shielding effect, the electric
180 potential was gradually confined to the poleward part of the Region 2 FACs, and the pen-
181 etrating electric field equatorward of the Region-2 FACs weakened. The direct impact
182 of this electric field pattern change is the formation of intense plasma flows at the bound-
183 ary between the Region-1 and Region-2 FACs, commonly referred to as the Birkeland
184 Current Boundary Flows (BCBF) (Archer et al., 2017; Archer & Knudsen, 2018). As-
185 sociated with the boundary flows are increased electric field/velocity gradients on both
186 sides. The BCBF flow may transport the low density plasma from the nightside to the
187 dayside and also gradually erode the high density SED plume through enhanced frictional
188 heating. As a result, a patch is segmented from the SED base. It is subsequently trans-
189 ported across the OCB and into the polar cap.

190 3 Discussion

191 SED segmentations were previously found to be related with the temporal change
192 of IMF B_y and B_z (e.g. Anderson et al., 1988; Milan et al., 2002; Sojka et al., 1993) or
193 transient reconnection (Carlson et al., 2006, 2004; Lockwood & Carlson, 1992). In this
194 case, between 2100 UT and 2300 UT, both IMF B_y and B_z were quite steady, ruling out
195 the possibility of temporal changes of the IMF.

196 To gain further insight into the magnetospheric origin of convection flows cutting
197 the patch, a 3-D view of the simulated magnetospheric configuration at 2300 UT when
198 the SED is segmented is shown in Figure 3. Color contours of plasma thermal pressure
199 are shown in the cut plane XY at $Z=-1$ RE. Colors on the sphere at 3 RE are contours
200 of the FACs (positive values mean upward FACs). Three white lines represent the sam-
201 ple field lines at the center of the SED base (MLAT=57.3, MLT=15.0), center of the bound-
202 ary flows (MLAT=63.0, MLT=13.8), and patch (MLAT=63.5, MLT=13.4). The center
203 of the SED base is where the electron density at 350 km reaches the local maximum, the
204 center of the boundary flow is where the electron density reaches the local minimum, and
205 similarly the center of patch is where the density reaches local maximum. The footprints
206 of these magnetic field lines are marked as white stars in Figure 2. The polar cap patch
207 was on open magnetic field lines and connected to the solar wind, showing that its pole-
208 ward movement was due to the magnetospheric convection driven by the southward IMF.
209 The SED base was mapped to the inner edge of the partial ring current, where the under-
210 shielded electric field was responsible for the SED lifting and TEC growth. This also ex-
211 plains why the SED base stopped providing plasma to the auroral region after the shield-
212 ing further developed. The boundary flow region was mapped to the outer boundary of
213 the partial ring current (poleward boundary of Region 2 FACs in the ionosphere). This
214 proves that the segmentation was due to the boundary flows located between the Re-
215 gion 1 and Region 2 FACs.

216 We further investigate how the boundary flows segment the SED plume into a patch.
 217 The plasma parcel at the center of the boundary flow at 2300 UT was traced backward
 218 in time to 2130 UT to identify its source region. The center of the boundary flow is lo-
 219 cated at MLAT=63.0,MLT=13.8 and marked with a white star in Figure 4c. It also co-
 220 located with the minimum of the electron density. The altitude profile of the electron
 221 density at 2300 UT is represented by the blue curve in Figure 4d. When the plasma par-
 222 cel was traced back in time, it was found that the source region was located at MLAT=58.3,
 223 MLT=15.6 at 2130 UT and also marked with a star in Figure 4a. The plasma parcel ex-
 224 experienced two development phases, i.e., a growing phase and a decaying phase. The grow-
 225 ing phase started at 2130 UT and continued to 2225 UT. The corresponding altitude pro-
 226 files of the electron density at these two time cadences are represented by the red and
 227 black curves in Figure 4d, respectively. During the growing phase, the plasma was lifted
 228 to higher altitudes, i.e., the hmF2 increased from 270 km to 320 km. The lifting was found
 229 to be mainly due to projection of the northward convection flows in the vertical direc-
 230 tion. At the end of the growing phase, this plasma parcel was located at MLAT=60.1,MLT=15.0,
 231 indicated by the star near the equatorward boundary of the boundary flow shown in the
 232 central panel of Figure 4b. The electron density at the hmF2 (~ 300 km) reached its
 233 maximum of $4.09 \times 10^{11} m^{-3}$ at 2225 UT. The decaying phase started at 2225 UT and
 234 the electron density in the F-layer below 400 km region kept decreasing. The temporal
 235 evolution of the horizontal ion drift, electron density and ion temperature in the plasma
 236 parcel at around 350 km is shown in Figure 4e-g, respectively. The horizontal flow was
 237 mainly westward and increased during the whole period due to the constant southward
 238 IMF, continuously growing particle ring current and the associated Region-2 current sys-
 239 tem. The electron density reached the maximum at 2225 UT. After 2225 UT, the con-
 240 vection flow continued to increase, and the ion temperature also increased due to stronger
 241 frictional heating between the ions and neutrals, which also resulted in an electron den-
 242 sity decrease.

243 The loss mechanism is further quantified. When the plasma parcel moved from the
 244 source region to the boundary flow region, at 300 km (around hmF2) the velocity dif-
 245 ference between ion and neutral increased from ~ 100 m/s to ~ 600 m/s, the ion tem-
 246 perature increased from ~ 1400 K to ~ 1700 K, and the neutral temperature remained at ~ 1400
 247 K. Based on the temperature dependent dissociative recombination equations in St.-Maurice
 248 and Torr (1978), the charge exchange rate between O^+ and N_2 increases from $5.73 \times$
 249 $10^{-13} cm^3 s^{-1}$ to $9.91 \times 10^{-13} cm^3 s^{-1}$, when the ion temperature increases from ~ 1400
 250 K to ~ 1700 K. The N_2 density was $\sim 1.5 \times 10^{14} m^{-3}$ and O^+ density was $\sim 3 \times 10^{11} m^{-3}$
 251 in the model output. The production rate of NO^+ thus increased $1.88 \times 10^7 m^{-3} s^{-1}$.
 252 The total NO^+ conversion during the decaying phase (~ 35 min) is $4 \times 10^{10} m^{-3}$. Be-
 253 cause the recombination between NO^+ and e^- is rapid, the electron density loss should
 254 also be $4 \times 10^{10} m^{-3}$, which matches the amount of electron lost between 2225 UT and
 255 2300 UT in the model output. This simple calculation confirms that the enhanced chem-
 256 ical reaction within the enhanced boundary flows led to the electron density decrease and
 257 the segmentation of the SED plume into a patch.

258 There are several proposed patch segmentation mechanisms with convincing ev-
 259 idence reported in previous literature, which highlights the complicated nature of the high-
 260 latitude ionospheric electrodynamics. In this numerical simulation, the partial ring cur-
 261 rent formed has a single pressure peak and thus the associated FAC and flow pattern are
 262 relatively simple. However, the ring current can have fine structures (Buzulukova et al.,
 263 2010; Wei, Yu, & He, 2019) and the associated FAC and flow pattern can be more com-
 264 plicated, which can potentially lead to more structures in the segmented patch. A lo-
 265 cal maximum of the convection flow and a local density minimum at 2235 UT in Fig-
 266 ure 4e-g further confirms this idea.

4 Summary and Conclusions

A new segmentation mechanism of SED plume into polar cap patches is proposed through numerical model study. A simulation of the ionospheric response to the geomagnetic storm on Sep 7, 2017 has been carried out using the Global Ionosphere and Thermosphere Model (GITM) driven by the two-way coupled BATSUS and RCM within SWMF. The simulation results are validated by comparison to GPS TEC observations and SYM-H index.

During storm time, dense SED plasma from the mid-latitude ionosphere is transported by the expanded two-cell convection pattern into the high-latitude region to form the SED plume. Meanwhile, plasma from the plasma sheet is transported into the inner magnetosphere by strong earthward convection and forms a strong partial ring current centered on the nightside. The partial ring current closes through the Region 2 FACs and gradually shields the subauroral region from the high-latitude penetrating electric fields. As the partial ring current grows, the shielding effect strengthens, causing the boundary flows between the Region 1 and Region 2 FACs to increase. This leads to enhanced ion temperature and chemical recombination rate, and thus reduced electron density. When the center of the partial ring current drifts westward due to the gradient and curvature drifts, these large boundary flows also move westward from the night side to the day side. When they encounter the SED plume, the plume is segmented into a patch, which later move further into the polar cap. During this process, no IMF variations or transient reconnections are required. The segmentation mechanism is entirely due to magnetospheric internal processes.

Acknowledgments

This work is supported by NASA Grant NNX14AF31G, FINESST 19-HELIO19-0021 and NSF Grant AGS1400998. The GPS TEC data used are available at the Madrigal database <http://millstonehill.haystack.mit.edu/>. We appreciate Dr. A. Coster for making this dataset available for use. The solar wind, IMF and Sym-H data are obtained from the NASA Omni web. The simulation results for the three selected time cadences are available at doi:10.7302/9097-z311.

References

- Aa, E., Huang, W., Liu, S., Ridley, A., Zou, S., Shi, L., ... Wang, T. (2018). Mid-latitude Plasma Bubbles Over China and Adjacent Areas During a Magnetic Storm on 8 September 2017. *Space Weather*, *16*(3), 321–331. doi: 10.1002/2017SW001776
- Anderson, D. N., Buchau, J., & Heelis, R. A. (1988). Origin of density enhancements in the winter polar cap ionosphere. *Radio Science*, *23*(4), 513–519. doi: 10.1029/RS023i004p00513
- Archer, W. E., Knudsen, D., Burchill, J., Jackel, B., Donovan, E., Connors, M., & Juusola, L. (2017). Birkeland current boundary flows. *Journal of Geophysical Research: Space Physics*, *122*(4), 4617–4627.
- Archer, W. E., & Knudsen, D. J. (2018). Distinguishing Subauroral Ion Drifts From Birkeland Current Boundary Flows. *Journal of Geophysical Research: Space Physics*, *123*(1), 819–826. doi: 10.1002/2017JA024577
- Buzulukova, N., Fok, M.-C., Pulkkinen, A., Kuznetsova, M., Moore, T. E., Glocer, A., ... Rastaetter, L. (2010). Dynamics of Ring Current and Electric Fields in the Inner Magnetosphere During Disturbed Periods: CRCM-BATS-R-US Coupled Model. *Journal of Geophysical Research : Space Physics*, *115*, 1–19. doi: 10.1029/2009JA014621
- Carlson, H. C., Moen, J., Oksavik, K., Nielsen, C. P., McCrea, I. W., Pedersen, T. R., & Gallop, P. (2006). Direct observations of injection events of subau-

- 317 ral plasma into the polar cap. *Geophysical Research Letters*, *33*(5), 5–8. doi:
318 10.1029/2005GL025230
- 319 Carlson, H. C., Oksavik, K., Moen, J., & Pedersen, T. (2004). Ionospheric patch
320 formation: Direct measurements of the origin of a polar cap patch. *Geophysical*
321 *Research Letters*, *31*(8), 2–5. doi: 10.1029/2003GL018166
- 322 Chamberlin, P. C., Woods, T. N., & Eparvier, F. G. (2007). Flare irradiance spec-
323 tral model (FISM): Daily component algorithms and results. *Space Weather*,
324 *5*(7), 1–23. doi: 10.1029/2007SW000316
- 325 Chamberlin, P. C., Woods, T. N., & Eparvier, F. G. (2008). Flare irradiance spec-
326 tral model (FISM): Flare component algorithms and results. *Space Weather*,
327 *5*(7). doi: 10.1029/2007SW000316
- 328 De Zeeuw, D. L., Sazykin, S., Wolf, R. A., Gombosi, T. I., Ridley, A. J., & Tóth, G.
329 (2004). Coupling of a global MHD code and an inner magnetospheric model:
330 Initial results. *Journal of Geophysical Research: Space Physics*, *109*(A12),
331 1–14. doi: 10.1029/2003JA010366
- 332 Foster, J. C. (1984). INOSPHERIC SIGNATURES OF MAGNETOSPHERIC
333 CONVECTION. *Journal of Geophysical Research*, *89*(2), 855–865.
- 334 Foster, J. C. (1993). Storm time plasma transport at middle and high latitudes.
335 *Journal of Geophysical Research: Space Physics*, *98*(A2), 1675–1689. doi: 10
336 .1029/92ja02032
- 337 Fuller-Rowell, T. J., & Evans, D. S. (1987). Height-integrated Pedersen and
338 Hall conductivity patterns inferred from the TIROS-NOAA satellite data.
339 *Journal of Geophysical Research*, *92*(A7), 7606. Retrieved from [http://](http://doi.wiley.com/10.1029/JA092iA07p07606)
340 [doi: 10.1029/JA092iA07p07606](http://doi.wiley.com/10.1029/JA092iA07p07606) doi: 10.1029/JA092iA07p07606
- 341 Goodwin, L. V., Iserhienrhien, B., Miles, D. M., Patra, S., Meeren, C. V. D.,
342 Buchert, S. C., ... Moen, J. (2015). Swarm in situ observations of
343 F region polar cap patches. *Geophysical Research Letters*, 1–8. doi:
344 10.1002/2014GL062610.High-resolution
- 345 Heelis, R. A., Sojka, J. J., David, M., & Schunk, R. W. (2009). Storm time density
346 enhancements in the middle-latitude dayside ionosphere. *Journal of Geophys-
347 ical Research: Space Physics*, *114*(3), 1–7. doi: 10.1029/2008JA013690
- 348 Jin, H., Zou, S., Chen, G., Yan, C., Zhang, S., & Yang, G. (2018). Formation
349 and Evolution of Low-Latitude F Region Field-Aligned Irregularities Dur-
350 ing the 7?8 September 2017 Storm: Hainan Coherent Scatter Phased Array
351 Radar and Digisonde Observations. *Space Weather*, *16*(6), 648–659. doi:
352 10.1029/2018SW001865
- 353 Lockwood, M., & Carlson, H. C. (1992). PRODUCTION OF POLAR CAP ELEC-
354 TRON DENSITY PATCHES BY TRANSIENT MAGNETOPOUSE RECON-
355 NECTION. *Geophys. Res. Lett.*, *19*(17), 1731–1734.
- 356 Milan, S. E., Lester, M., & Yeoman, T. K. (2002). HF radar polar patch forma-
357 tion revisited: Summer and winter variations in dayside plasma structuring.
358 *Annales Geophysicae*, *20*(4), 487–499. doi: 10.5194/angeo-20-487-2002
- 359 Moen, J., Carlson, H. C., Oksavik, K., Nielsen, C. P., Pryse, S. E., Middleton,
360 H. R., ... Gallop, P. (2006). EISCAT observations of plasma patches at
361 sub-auroral cusp latitudes. *Annales Geophysicae*, *24*(9), 2363–2374. doi:
362 10.5194/angeo-24-2363-2006
- 363 Ogawa, T., Buchert, S. C., Nishitani, N., Sato, N., & Lester, M. (2001). Plasma den-
364 sity suppression process around the cusp revealed by simultaneous CUTLASS
365 and EISCAT Svalbard radar observations. *Journal of Geophysical Research:
366 Space Physics*, *106*(A4), 5551–5564. doi: 10.1029/2000ja900111
- 367 Oksavik, K., Greenwald, R. A., Ruohoniemi, J. M., Hairston, M. R., Paxton, L. J.,
368 Baker, J. B. H., ... Barnes, R. J. (2006). First observations of the tempo-
369 ral/spatial variation of the sub-auroral polarization stream from the Super-
370 DARN Wallops HF radar. *Geophysical Research Letters*, *33*(12), 1–5. doi:
371 10.1029/2006GL026256

- 372 Østgaard, N., Vondrak, R. R., Gjerloev, J. W., & Germany, G. (2002). A relation
373 between the energy deposition by electron precipitation and geomagnetic
374 indices during substorms. *Journal of Geophysical Research: Space Physics*,
375 *107*(A9), 1–7. doi: 10.1029/2001JA002003
- 376 Pinnock, M., Rodger, A. S., Dudeney, J. R., Baker, K. B., Newell, P. T., Greenwald,
377 R. A., & Greenspan, M. E. (1993). Observations of an enhanced convec-
378 tion channel in the cusp ionosphere. *Journal of Geophysical Research: Space*
379 *Physics*, *98*(A3), 3767–3776. doi: 10.1029/92ja01382
- 380 Ren, J., Zou, S., Gillies, R. G., Donovan, E., & Varney, R. H. (2018). Statis-
381 tical Characteristics of Polar Cap Patches Observed by RISR-C. *Jour-*
382 *nal of Geophysical Research: Space Physics*, *123*(8), 6981–6995. doi:
383 10.1029/2018JA025621
- 384 Ridley, A. J., Deng, Y., & Tóth, G. (2006). The global ionosphere-thermosphere
385 model. *Journal of Atmospheric and Solar-Terrestrial Physics*, *68*(8), 839–864.
386 doi: 10.1016/j.jastp.2006.01.008
- 387 Rodger, A. S., Pinnock, M., Dudeney, J. R., Baker, K. B., & Greenwald, R. A.
388 (1994). A new mechanism for polar patch formation. *Journal of Geo-*
389 *physical Research: Space Physics*, *99*(A4), 6425–6436. Retrieved from
390 <http://dx.doi.org/10.1029/93JA01501> doi: 10.1029/93JA01501
- 391 Shen, C., Luo, B., Chi, Y., Xu, M., & Wang, Y. (2018). Why the Shock-ICME Com-
392 plex Structure Is Important: Learning from the Early 2017 September CMEs.
393 *The Astrophysical Journal*, *861*(1), 28. Retrieved from [http://dx.doi.org/](http://dx.doi.org/10.3847/1538-4357/aac204)
394 [10.3847/1538-4357/aac204](http://dx.doi.org/10.3847/1538-4357/aac204) doi: 10.3847/1538-4357/aac204
- 395 Sojka, J. J., Bowline, M. D., Schunk, R. W., Decker, D. T., Valladares, C. E., Shee-
396 han, R., ... Heelis, R. A. (1993). Modeling polar cap F[?]region patches using
397 time varying convection. *Geophysical Research Letters*, *20*(17), 1783–1786. doi:
398 10.1029/93GL01347
- 399 St.-Maurice, J. P., & Torr, D. G. (1978). Nonthermal rate coefficients in the iono-
400 sphere: The reactions of O + With N₂, O₂, and NO. *Journal of Geophysi-*
401 *cal Research*, *83*(A12), 5779. doi: 10.1029/ja083ia12p05779
- 402 Tóth, G., Sokolov, I. V., Gombosi, T. I., Chesney, D. R., Clauer, C. R., De Zeeuw,
403 D. L., ... Kóta, J. (2005). Space weather modeling framework: A new tool for
404 the space science community. *Journal of Geophysical Research: Space Physics*,
405 *110*(A12), 1–21. doi: 10.1029/2005JA011126
- 406 Tóth, G., Van der Holst, B., Sokolov, I. V., De Zeeuw, D. L., Gombosi, T. I., Fang,
407 F., ... others (2012). Adaptive numerical algorithms in space weather model-
408 ing. *Journal of Computational Physics*, *231*(3), 870–903.
- 409 Valladares, C. E., Basu, S., Buchau, J., & Friis-Christensen, E. (1994). Experimen-
410 tal evidence for the formation and entry of patches into the polar cap. *Radio*
411 *Science*, *29*(1), 167–194. doi: 10.1029/93RS01579
- 412 Valladares, C. E., Decker, D. T., Sheehan, R., & Anderson, D. N. (1996). Model-
413 ing the formation of polar cap patches using large plasma flows. *Radio Science*,
414 *31*(3), 573–593. doi: 10.1029/96RS00481
- 415 Vasyliunas, V. (1970). *Mathematical Models of Magnetospheric Convection and its*
416 *Coupling to the Ionosphere* (Vol. 17).
- 417 Walker, I. K., Moen, J., Kersley, L., & Lorentzen, D. A. (1999). On the possible role
418 of cusp/cleft precipitation in the formation of polar-cap patches. *Annales Geo-*
419 *physicae*, *17*(10), 1298–1305. doi: 10.1007/s00585-999-1298-4
- 420 Wei, D., Yu, Y., & He, F. (2019). The magnetospheric driving source of double-peak
421 subauroral ion drifts (dsoids): Double ring current pressure peaks. *Geophysical*
422 *Research Letters*, *0*(ja).
- 423 Weimer, D. R. (2005). Improved ionospheric electrodynamic models and applica-
424 tion to calculating Joule heating rates. *Journal of Geophysical Research: Space*
425 *Physics*, *110*(A5), 1–21. doi: 10.1029/2004JA010884
- 426 Wolf, R. A., Spiro, R. W., Sazykin, S., & Toffoletto, F. R. (2007). How the Earth's

- 427 inner magnetosphere works: An evolving picture. *Journal of Atmospheric and*
428 *Solar-Terrestrial Physics*, 69(3), 288–302. doi: 10.1016/j.jastp.2006.07.026
- 429 Zhang, Q. H., Moen, J., Lockwood, M., McCrea, I. W., Zhang, B. C., McWilliams,
430 K. A., ... Lester, M. (2016). Polar cap patch transportation beyond the classic
431 scenario. *Journal of Geophysical Research : Space Physics*, 121(9), 9063–9074.
- 432 Zhang, Q. H., Zhang, B. C., Liu, R. Y., Dunlop, M. W., Lockwood, M., Moen, J.,
433 ... Lester, M. (2011). On the importance of interplanetary magnetic field By
434 on polar cap patch formation. *Journal of Geophysical Research: Space Physics*,
435 116(5), 1–13. doi: 10.1029/2010JA016287
- 436 Zhang, Q. H., Zhang, B. C., Moen, J., Lockwood, M., McCrea, I. W., Yang, H. G.,
437 ... Lester, M. (2013). Polar cap patch segmentation of the tongue of ion-
438 ization in the morning convection cell. *Geophysical Research Letters*, 40(12),
439 2918–2922. doi: 10.1002/grl.50616
- 440 Zou, S., Moldwin, M. B., Ridley, A. J., Nicolls, M. J., Coster, A. J., Thomas, E. G.,
441 & Ruohoniemi, J. M. (2014). On the generation/decay of the storm-enhanced
442 density plumes: Role of the convection flow and field-aligned ion flow. *Jour-*
443 *nal of Geophysical Research: Space Physics*, 119(10), 8543–8559. Retrieved
444 from [https://agupubs.onlinelibrary.wiley.com/doi/abs/10.1002/](https://agupubs.onlinelibrary.wiley.com/doi/abs/10.1002/2014JA020408)
445 [2014JA020408](https://agupubs.onlinelibrary.wiley.com/doi/abs/10.1002/2014JA020408) doi: 10.1002/2014JA020408
- 446 Zou, S., Ridley, A. J., Moldwin, M. B., Nicolls, M. J., Coster, A. J., Thomas, E. G.,
447 & Ruohoniemi, J. M. (2013). Multi-instrument observations of SED dur-
448 24–25 October 2011 storm: Implications for SED formation processes.
449 *Journal of Geophysical Research: Space Physics*, 118(12), 7798–7809. doi:
450 10.1002/2013JA018860

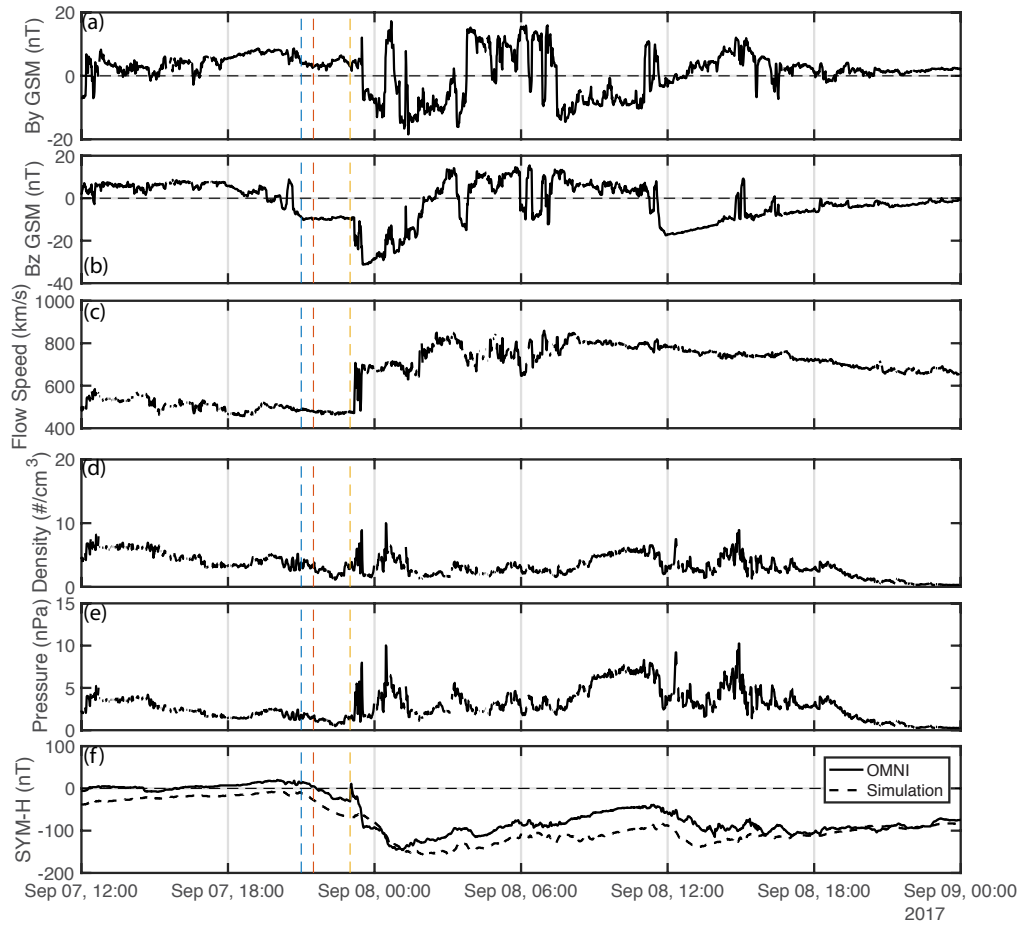


Figure 1. Solar wind data and geomagnetic index from 12 UT Sep 7 to 0 UT Sep 9, 2017. (a) IMF By component in the GSM coordinates, (b) IMF Bz component in the GSM coordinates, (c) solar wind speed, (d) proton number density, (e) solar wind dynamic pressure, and (f) the SYM-H index (solid line) and simulated Dst index (dash line). The color-coded vertical dashed lines indicate timing of the three snapshots in Figure 2.

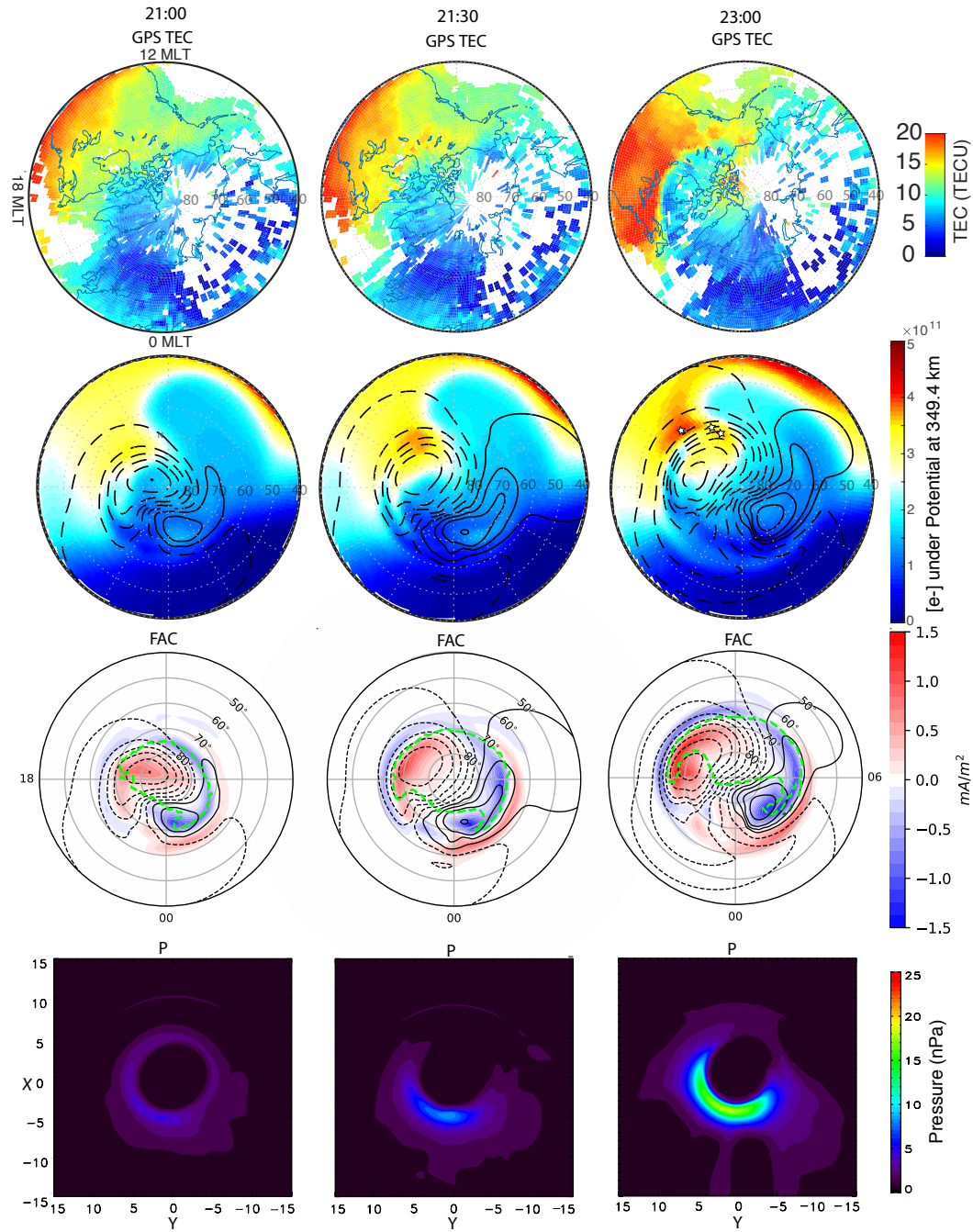


Figure 2. First row: Polar view of TEC in the geomagnetic coordinates. Second row: Polar view of modeled electron density (color contours) at 349.4 km under electric equipotential (contour lines) in the geomagnetic coordinates. The SED base, boundary flow and polar cap patch are marked with stars at 23 UT. Third row: Polar view of the modeled FACs (color contours) under electric equipotential (contour lines) in the geomagnetic coordinates. The green dashed line represents the open-closed field line boundary. Fourth row: the modeled plasma thermal pressure in the $z=0$ plane in the GSM coordinates.

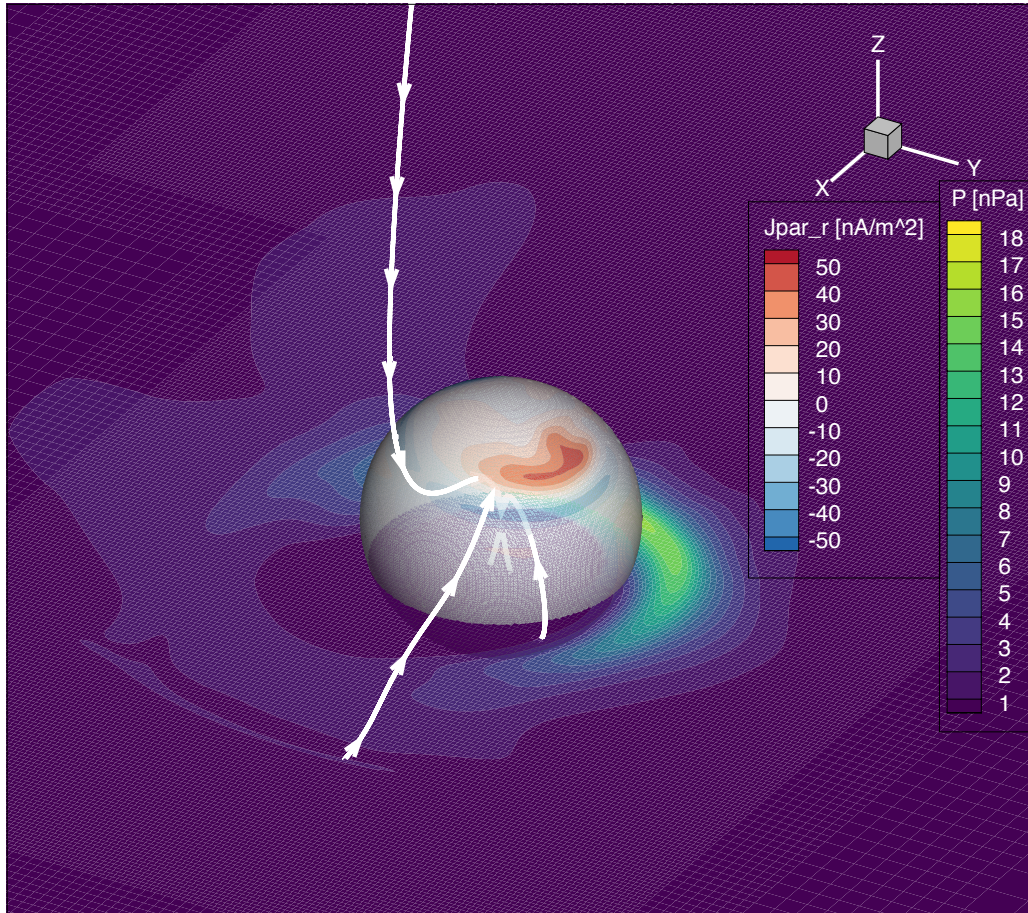


Figure 3. A 3-D view of the simulated magnetosphere extracted from the time step when SED was segmented at 23 UT. Shown in the cut plane XY at $Z = -1$ RE are color contours of the plasma thermal pressure. Color contours on the sphere with a radius of 3 RE indicate the field-aligned current density (positive values mean upward field-aligned currents). Three white lines represent the sample magnetic field lines at the SED base (the lowest lat.), boundary flow (the middle lat.) and patch (the highest lat.) around this time. The foot prints of these magnetic field lines are shown as stars in Figure 2.

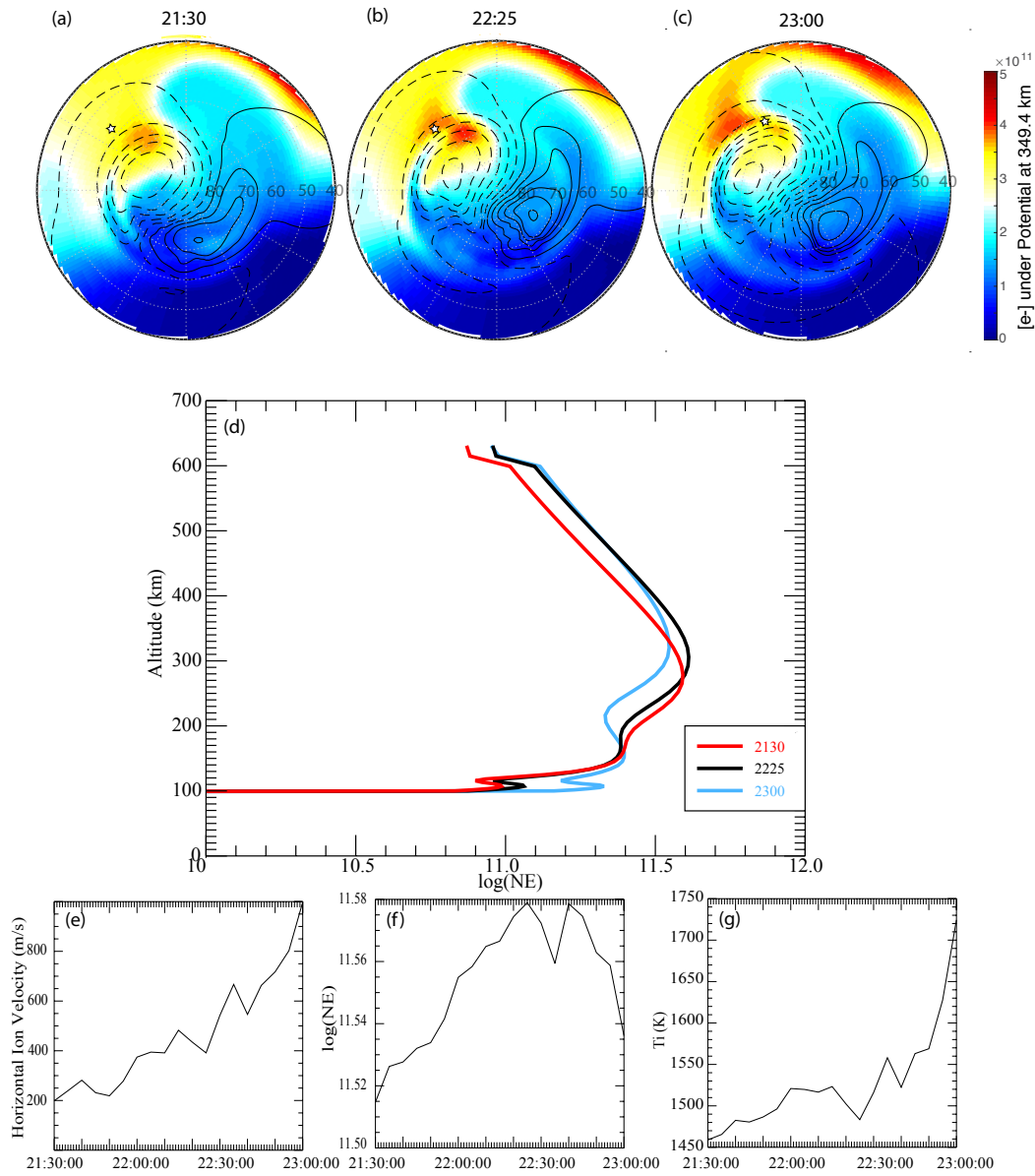


Figure 4. One simulation plasma parcel is traced backward in time. The locations of the plasma parcel and altitude profiles of the electron density at three different time cadences are shown. (a)-(c) Polar view of the F-region electron density and the locations of the traced plasma parcel are marked with stars at 2130, 2225 and 2300 UT, respectively. The format of polar view plots of the electron density is the same as the second row in Figure 2. (d) The red curve indicates the initial density profile at 2130 UT, the black curve indicates the density profile at the end of the growing phase, i.e., 2225 UT, and the blue curve indicates the density profile at the end of the decaying phase, i.e., 2300 UT. (e)-(g) The temporal evolution of the horizontal ion drift, electron density and ion temperature in the plasma parcel at around 300 km.

Figure 1.

Author Manuscript

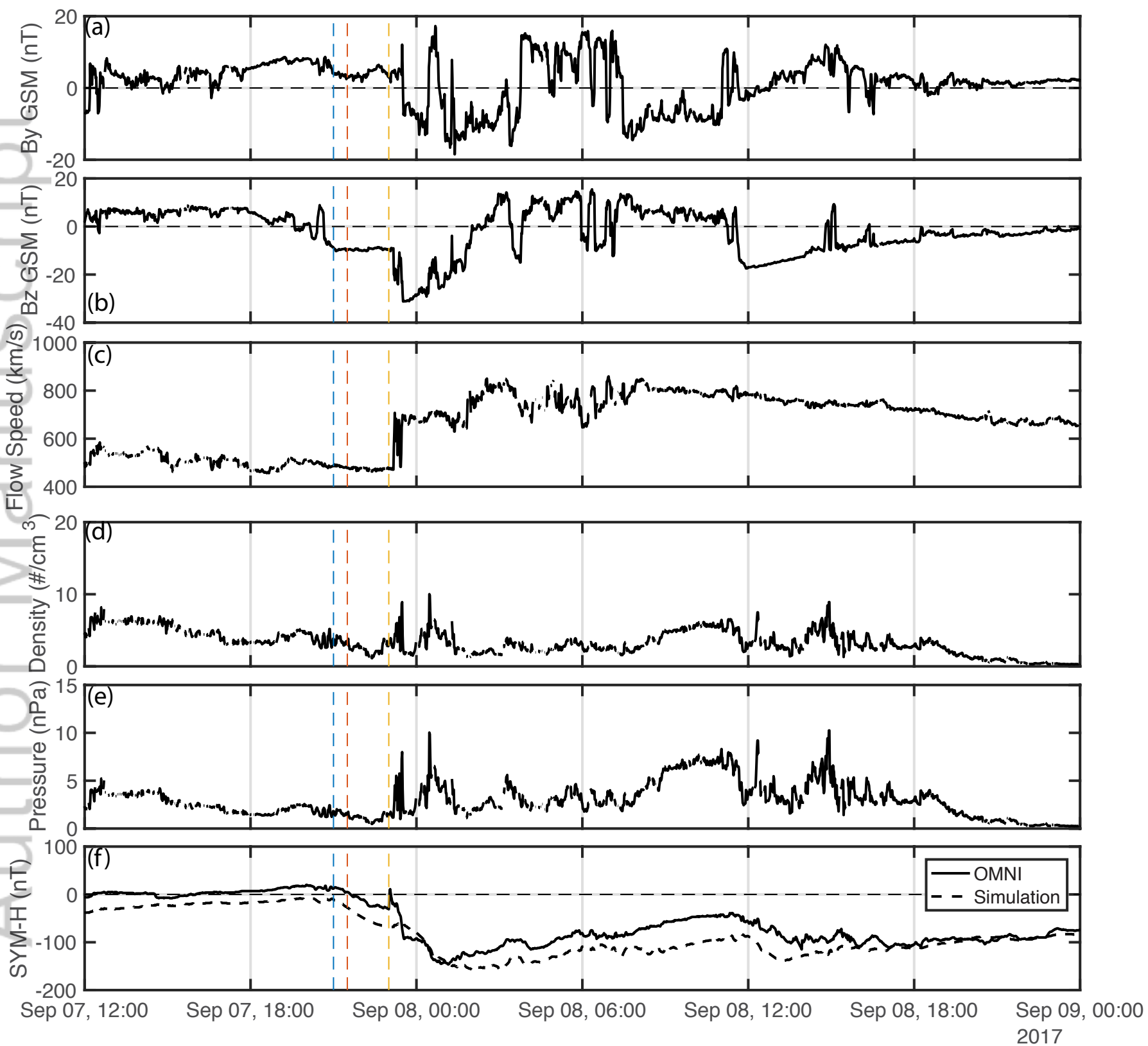


Figure 2.

Author Manuscript

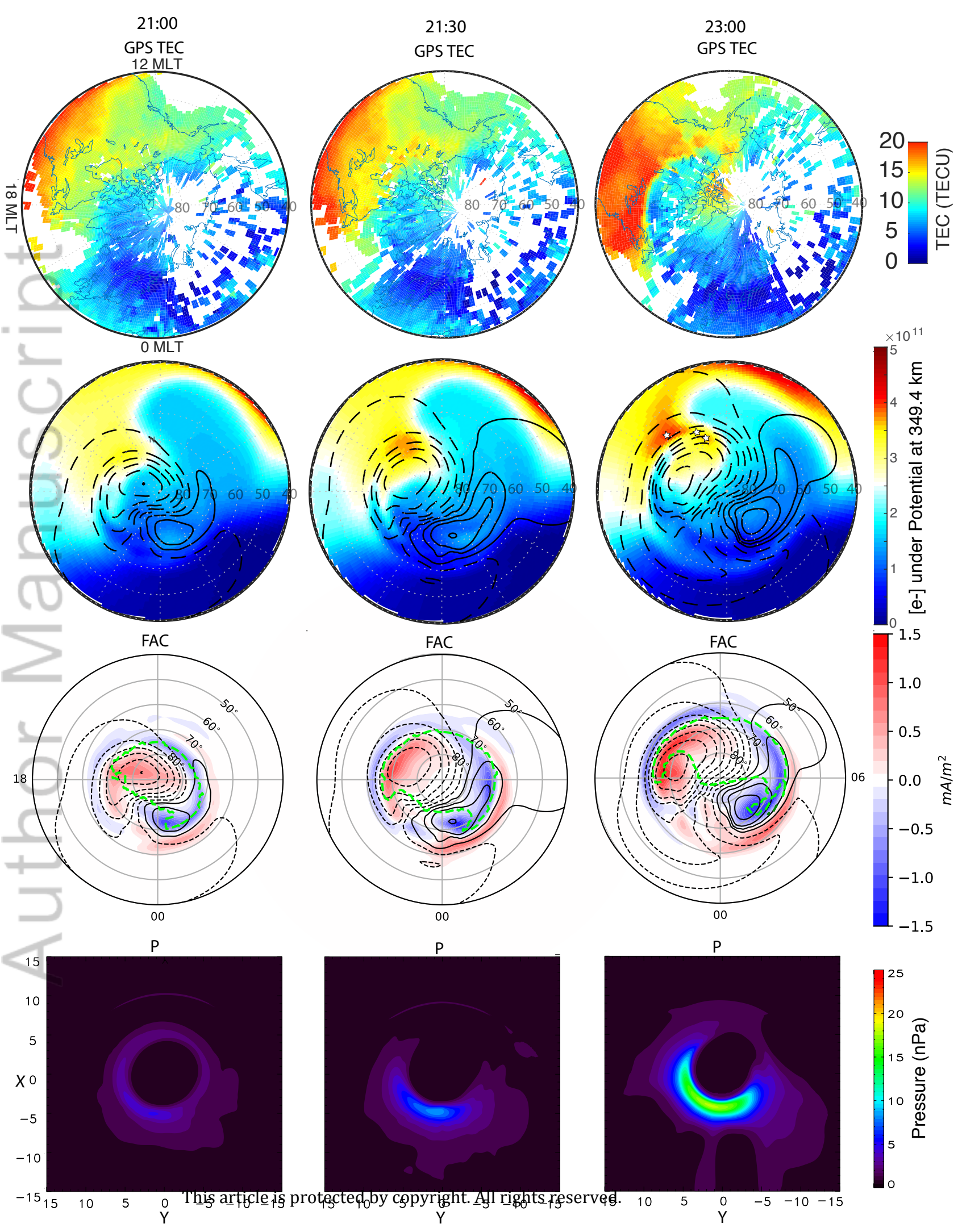


Figure 3.

Author Manuscript

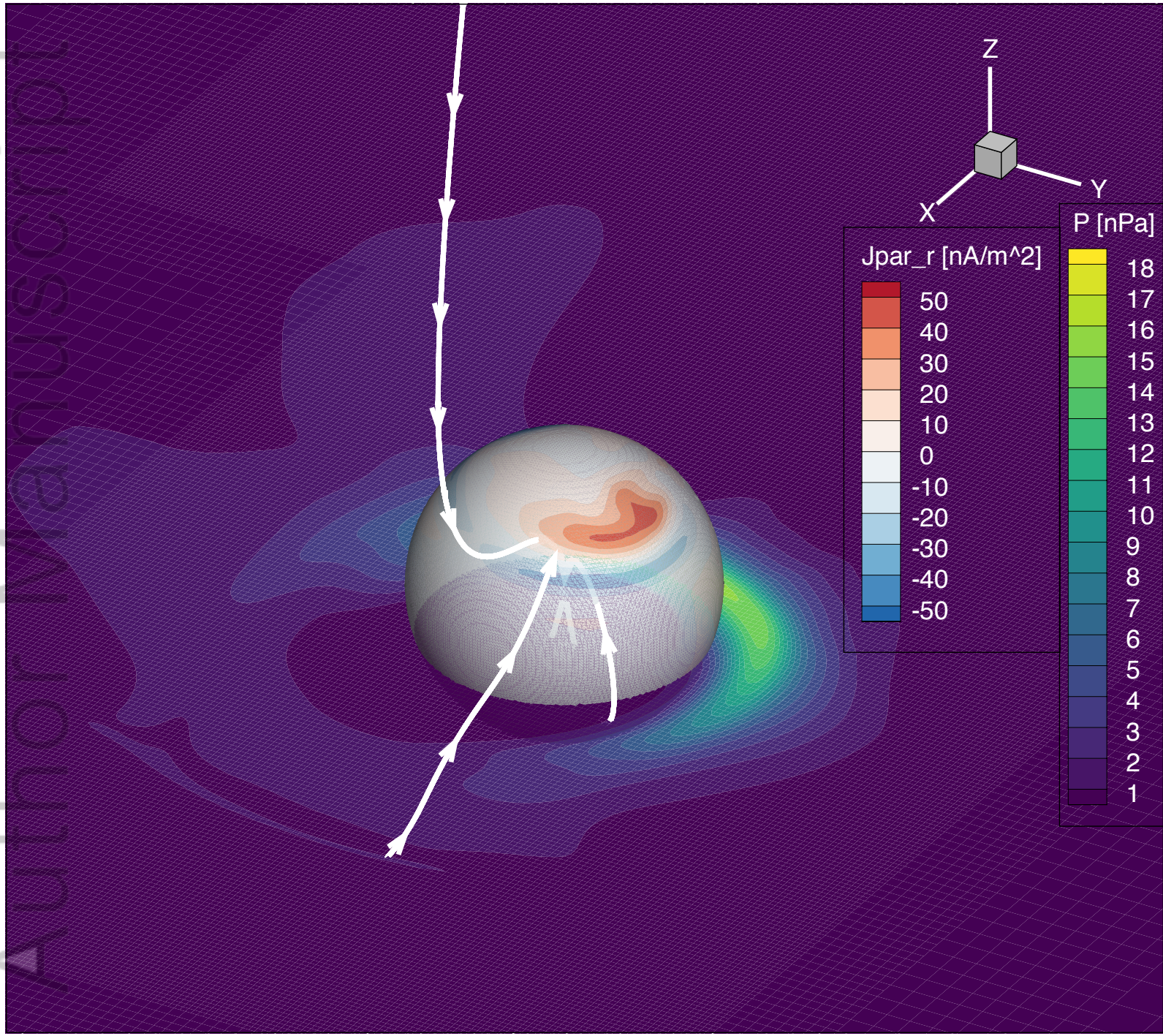


Figure 4.

Author Manuscript

